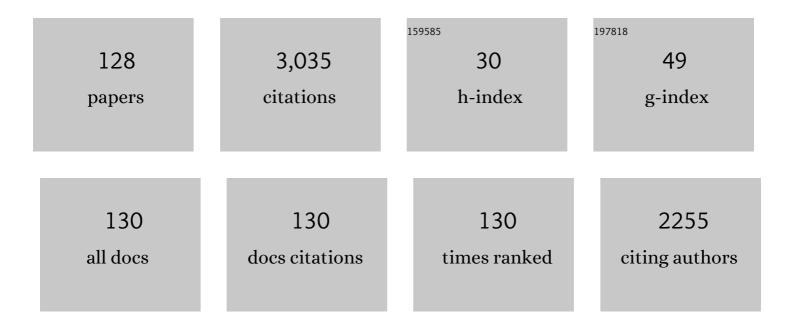
Yuji Higo

List of Publications by Year in descending order

Source: https://exaly.com/author-pdf/4417228/publications.pdf Version: 2024-02-01



#	Article	IF	CITATIONS
1	Stability of hydrous silicate at high pressures and water transport to the deep lower mantle. Nature Geoscience, 2014, 7, 224-227.	12.9	259
2	Sound velocities of majorite garnet and the composition of the mantle transition region. Nature, 2008, 451, 814-817.	27.8	130
3	Pâ¿¢Vâ¿¢T relation of MgO derived by simultaneous elastic wave velocity and in situ X-ray measurements: A new pressure scale for the mantle transition region. Physics of the Earth and Planetary Interiors, 2010, 183, 196-211.	1.9	113
4	Semidilute region for linear polymers in good solvents. Macromolecules, 1984, 17, 1055-1059.	4.8	86
5	The system K2CO3-MgCO3 at 6 GPa and 900-1450 ÂC. American Mineralogist, 2013, 98, 1593-1603.	1.9	79
6	Effect of water on the spinel-postspinel transformation in Mg2SiO4. Geophysical Research Letters, 2001, 28, 3505-3508.	4.0	75
7	Osmotic Pressure of Semidilute Solutions of Branched Polymers. Polymer Journal, 1983, 15, 367-375.	2.7	69
8	Sound velocity of CaSiO3 perovskite suggests the presence of basaltic crust in the Earth's lower mantle. Nature, 2019, 565, 218-221.	27.8	66
9	Generation of pressures over 40 GPa using Kawai-type multi-anvil press with tungsten carbide anvils. Review of Scientific Instruments, 2016, 87, 024501.	1.3	64
10	Equation of state of \hat{I}^3 -Fe: Reference density for planetary cores. Earth and Planetary Science Letters, 2013, 375, 244-253.	4.4	60
11	The effect of iron on the elastic properties of ringwoodite at high pressure. Physics of the Earth and Planetary Interiors, 2006, 159, 276-285.	1.9	59
12	The phase boundary between wadsleyite and ringwoodite in Mg2SiO4 determined by in situ X-ray diffraction. Physics and Chemistry of Minerals, 2006, 33, 106-114.	0.8	58
13	Over 1 Mbar generation in the Kawai-type multianvil apparatus and its application to compression of (Mg0.92Fe0.08)SiO3 perovskite and stishovite. Physics of the Earth and Planetary Interiors, 2014, 228, 262-267.	1.9	55
14	Mantle dynamics inferred from the crystallographic preferred orientation of bridgmanite. Nature, 2016, 539, 81-84.	27.8	55
15	Elastic wave velocities of (Mg0.91Fe0.09)2SiO4 ringwoodite under P–T conditions of the mantle transition region. Physics of the Earth and Planetary Interiors, 2008, 166, 167-174.	1.9	54
16	High-pressure phase transitions in FeCr2O4 and structure analysis of new post-spinel FeCr2O4 and Fe2Cr2O5 phases with meteoritical and petrological implications. American Mineralogist, 2014, 99, 1788-1797.	1.9	54
17	Intermediate-depth earthquakes linked to localized heating in dunite and harzburgite. Nature Geoscience, 2017, 10, 771-776.	12.9	53
18	Dislocation-accommodated grain boundary sliding as the major deformation mechanism of olivine in the Earth's upper mantle. Science Advances, 2015, 1, e1500360.	10.3	49

#	Article	IF	CITATIONS
19	Simultaneous sound velocity and density measurements of NaCl at high temperatures and pressures: Application as a primary pressure standard. American Mineralogist, 2012, 97, 1670-1675.	1.9	48
20	P-V-T equation of state of CaCO3 aragonite to 29 GPa and 1673 K: In situ X-ray diffraction study. Physics of the Earth and Planetary Interiors, 2017, 265, 82-91.	1.9	48
21	Melting and subsolidus phase relations in the system Na2CO3-MgCO3ÂH2O at 6 GPa and the stability of Na2Mg(CO3)2 in the upper mantle. American Mineralogist, 2013, 98, 2172-2182.	1.9	47
22	A system for measuring elastic wave velocity under high pressure and high temperature using a combination of ultrasonic measurement and the multi-anvil apparatus at SPring-8. Journal of Synchrotron Radiation, 2009, 16, 762-768.	2.4	45
23	Thermal equation of state of Mg3Al2Si3O12 pyrope garnet up to 19ÂGPa and 1,700ÂK. Physics and Chemistry of Minerals, 2012, 39, 589-598.	0.8	41
24	Pressure and temperature dependences of elastic properties of grossular garnet up to 17 GPa and 1 650 K. Journal of Earth Science (Wuhan, China), 2010, 21, 782-791.	3.2	40
25	Phase Relations in the System MgSiO ₃ â€Al ₂ O ₃ up to 2300ÂK at Lower Mantle Pressures. Journal of Geophysical Research: Solid Earth, 2017, 122, 7775-7788.	3.4	40
26	In situ observation of a garnet/perovskite transition in CaGeO3. Physics and Chemistry of Minerals, 2011, 38, 735-740.	0.8	39
27	Pressure and Composition Effects on Sound Velocity and Density of Coreâ€Forming Liquids: Implication to Core Compositions of Terrestrial Planets. Journal of Geophysical Research E: Planets, 2019, 124, 2272-2293.	3.6	39
28	Sound velocities of Fe3Al2Si3O12 almandine up to 19 GPa and 1700 K. Physics of the Earth and Planetary Interiors, 2015, 246, 1-8.	1.9	38
29	Elastic wave velocities of silica glass at high temperatures and high pressures. Journal of Applied Physics, 2010, 107, .	2.5	35
30	Precise determination of the phase boundary between coesite and stishovite in SiO 2. Physics of the Earth and Planetary Interiors, 2017, 264, 1-6.	1.9	35
31	Towards a consensus on the pressure and composition dependence of sound velocity in the liquid Fe–S system. Physics of the Earth and Planetary Interiors, 2016, 257, 230-239.	1.9	31
32	Sharp 660-km discontinuity controlled by extremely narrow binary post-spinel transition. Nature Geoscience, 2019, 12, 869-872.	12.9	31
33	Elasticity and sound velocities of polycrystalline Mg3Al2(SiO4)3 garnet up to 20 GPa and 1700 K. Journa of Applied Physics, 2012, 112, .	2.5	30
34	Curious kinetic behavior in silica polymorphs solves seifertite puzzle in shocked meteorite. Science Advances, 2015, 1, e1500075.	10.3	29
35	Isothermal compression of face-centered cubic iron. American Mineralogist, 2012, 97, 1417-1420.	1.9	25
36	Pressure generation to 65â€GPa in a Kawai-type multi-anvil apparatus with tungsten carbide anvils. High Pressure Research, 2017, 37, 507-515.	1.2	25

Үијі Нісо

#	Article	IF	CITATIONS
37	Decomposition of kyanite and solubility of Al2O3 in stishovite at high pressure and high temperature conditions. Physics and Chemistry of Minerals, 2006, 33, 711-721.	0.8	24
38	In situ stress-strain measurements in a deformation-DIA apparatus at P-T conditions of the upper part of the mantle transition zone. American Mineralogist, 2011, 96, 1665-1672.	1.9	23
39	Sound velocity measurements in liquid Fe–S at high pressure: Implications for Earth's and lunar cores. Earth and Planetary Science Letters, 2013, 362, 182-186.	4.4	23
40	High-pressure and high-temperature phase diagram for Fe0.9Ni0.1–H alloy. Physics of the Earth and Planetary Interiors, 2014, 228, 192-201.	1.9	23
41	Synthesis of boron-doped diamond and its application as a heating material in a multi-anvil high-pressure apparatus. Review of Scientific Instruments, 2017, 88, 093904.	1.3	23
42	High-pressure generation in the Kawai-type multianvil apparatus equipped with tungsten-carbide anvils and sintered-diamond anvils, and X-ray observation on CaSnO3 and (Mg,Fe)SiO3. Comptes Rendus - Geoscience, 2019, 351, 253-259.	1.2	23
43	Hydrostatic Compression Behavior and High-Pressure Stabilized β-Phase in γ-Based Titanium Aluminide Intermetallics. Metals, 2016, 6, 165.	2.3	22
44	Effect of rareâ€earth ion size on elasticity and crack initiation in rareâ€earth aluminate glasses. Journal of the American Ceramic Society, 2018, 101, 5030-5036.	3.8	22
45	Transition from melting to carbonization of naphthalene, anthracene, pyrene and coronene at high pressure. Physics of the Earth and Planetary Interiors, 2017, 270, 29-39.	1.9	21
46	In situ observation of a phase transition in Fe2SiO4 at high pressure and high temperature. Physics and Chemistry of Minerals, 2013, 40, 811-816.	0.8	20
47	Sound velocities measurement on MgSiO3 akimotoite at high pressures and high temperatures with simultaneous in situ X-ray diffraction and ultrasonic study. Physics of the Earth and Planetary Interiors, 2014, 228, 97-105.	1.9	20
48	High-Pressure–High-Temperature Study of Benzene: Refined Crystal Structure and New Phase Diagram up to 8 GPa and 923 K. Crystal Growth and Design, 2018, 18, 3016-3026.	3.0	20
49	Effect of pressure on temperature measurements using WRe thermocouple and its geophysical impact. Physics of the Earth and Planetary Interiors, 2020, 298, 106348.	1.9	20
50	Pressure-induced amorphization of a dense coordination polymer and its impact on proton conductivity. APL Materials, 2014, 2, .	5.1	19
51	Sound velocity and elastic properties of Fe–Ni and Fe–Ni–C liquids at high pressure. Physics and Chemistry of Minerals, 2016, 43, 229-236.	0.8	19
52	Unusual Pressure Effect on the Shear Modulus in MgAl2O4 Spinel. Journal of Physical Chemistry C, 2013, 117, 24518-24526.	3.1	18
53	In situ observation of crystallographic preferred orientation of deforming olivine at high pressure and high temperature. Physics of the Earth and Planetary Interiors, 2015, 243, 1-21.	1.9	17
54	Exploratory study of the new B-doped diamond heater at high pressure and temperature and its application to in situ XRD experiments on hydrous Mg-silicate melt. High Pressure Research, 2008, 28, 255-264.	1.2	16

Үијі Нісо

#	Article	IF	CITATIONS
55	P–V–T equation of state of siderite to 33 GPa and 1673 K. Physics of the Earth and Planetary Interiors, 2013, 224, 83-87.	1.9	16
56	Elastic wave velocity of polycrystalline Mj80Py20 garnet to 21ÂGPa and 2,000ÂK. Physics and Chemistry of Minerals, 2015, 42, 213-222.	0.8	16
57	Sound velocities of aluminumâ€bearing stishovite in the mantle transition zone. Geophysical Research Letters, 2016, 43, 4239-4246.	4.0	16
58	Solid Solution and Compression Behavior of Hydroxides in the Lower Mantle. Journal of Geophysical Research: Solid Earth, 2019, 124, 10231-10239.	3.4	16
59	Ultrafine spherulite Mg alloy with high yield strength. Journal of Alloys and Compounds, 2019, 784, 1284-1289.	5.5	16
60	Hydrogenation of FeSi under high pressure. American Mineralogist, 2011, 96, 93-99.	1.9	15
61	Sound velocities of MORB and absence of a basaltic layer in the mantle transition region. Geophysical Research Letters, 2012, 39, .	4.0	15
62	Stability and Solubility of the FeAlO ₃ Component in Bridgmanite at Uppermost Lower Mantle Conditions. Journal of Geophysical Research: Solid Earth, 2020, 125, e2019JB018447.	3.4	15
63	Depressed 660-km discontinuity caused by akimotoite–bridgmanite transition. Nature, 2022, 601, 69-73.	27.8	15
64	Phase transitions of serpentine in the lower mantle. Physics of the Earth and Planetary Interiors, 2015, 245, 52-58.	1.9	14
65	Exsolution kinetics of majoritic garnet from clinopyroxene in subducting oceanic crust. Physics of the Earth and Planetary Interiors, 2011, 189, 47-55.	1.9	13
66	Phase relations in the carbon-saturated C–Mg–Fe–Si–O system and C and Si solubility in liquid Fe at high pressure and temperature: implications for planetary interiors. Physics and Chemistry of Minerals, 2013, 40, 647-657.	0.8	13
67	Creep strength of ringwoodite measured at pressure–temperature conditions of the lower part of the mantle transition zone using a deformation–DIA apparatus. Earth and Planetary Science Letters, 2016, 454, 10-19.	4.4	13
68	Effect of sulfur on sound velocity of liquid iron under Martian core conditions. Nature Communications, 2020, 11, 1954.	12.8	13
69	High-Pressure and High-Temperature Stability and Equation of State of Superhydrous Phase B. Geophysical Monograph Series, 2013, , 147-157.	0.1	12
70	Deformation-induced crystallographic-preferred orientation of hcp-iron: An experimental study using a deformation-DIA apparatus. Earth and Planetary Science Letters, 2018, 490, 151-160.	4.4	12
71	Thermal equation of state of MgSiO4H2 phase H determined by in situ X-ray diffraction and a multianvil apparatus. Physics and Chemistry of Minerals, 2018, 45, 995-1001.	0.8	12
72	Development of a New Suppressor for the Ion Chromatography of Inorganic Cations. Analytical Sciences, 2014, 30, 477-482.	1.6	11

#	Article	IF	CITATIONS
73	Compressibilities of MnFe2O4 polymorphs. Physics and Chemistry of Minerals, 2015, 42, 569-577.	0.8	11
74	Compressional and shear wave velocities for polycrystalline <i>bcc</i> -Fe up to 6.3 GPa and 800 K. American Mineralogist, 2016, 101, 1150-1160.	1.9	11
75	Thermoelastic properties of chromium oxide Cr2O3 (eskolaite) at high pressures and temperatures. Physics and Chemistry of Minerals, 2016, 43, 447-458.	0.8	11
76	High-pressure X-ray diffraction and Raman spectroscopy of CaFe2O4-type β-CaCr2O4. Physics and Chemistry of Minerals, 2016, 43, 307-314.	0.8	11
77	Grain growth of Îμ -iron: Implications to grain size and its evolution in the Earth's inner core. Earth and Planetary Science Letters, 2017, 459, 238-243.	4.4	11
78	High-Pressure Phase Diagrams of Na2CO3 and K2CO3. Minerals (Basel, Switzerland), 2019, 9, 599.	2.0	11
79	Viscosity of bridgmanite determined by in situ stress and strain measurements in uniaxial deformation experiments. Science Advances, 2022, 8, eabm1821.	10.3	11
80	Phase boundary between perovskite and post-perovskite structures in MnGeO3 determined by in situ X-ray diffraction measurements using sintered diamond anvils. American Mineralogist, 2011, 96, 89-92.	1.9	10
81	Determination of pressure effect on thermocouple electromotive force using multi-anvil apparatus. High Pressure Research, 2016, 36, 121-139.	1.2	10
82	Lattice parameter evolution during heating of Ti-45Al-7.5Nb-0.25/0.5C alloys under atmospheric and high pressures. Intermetallics, 2018, 102, 120-131.	3.9	10
83	Phase transition of wadsleyite-ringwoodite in the Mg2SiO4-Fe2SiO4 system. American Mineralogist, 2019, 104, 588-594.	1.9	10
84	Sound velocity measurements of ε–FeOOH up to 24 GPa. Journal of Mineralogical and Petrological Sciences, 2019, 114, 155-160.	0.9	9
85	Repulsive Nature for Hydrogen Incorporation to Fe3C up to 14 GPa. ISIJ International, 2014, 54, 2637-2642.	1.4	9
86	Preparation and Characterization of a Poly(strong base) with Narrow Molecular Weight Distribution; Poly(4-vinylbenzyltrimethylammonium chloride). Polymer Journal, 1980, 12, 729-734.	2.7	8
87	Gel-Permeation Chromatography and Intrinsic Viscosity of Poly(4-vinylbenzyltrimethylammonium) Tj ETQq1 1 0.	784314 rg 2.7	;BT ₈ /Overlock
88	Stress relaxation experiments of olivine under conditions of subducted slab in Earth's deep upper mantle. Physics of the Earth and Planetary Interiors, 2010, 183, 164-174.	1.9	8
89	Sound Velocities of Alâ€Bearing Phase D up to 22ÂGPa and 1300ÂK. Geophysical Research Letters, 2020, 47, e2020GL088877.	4.0	8
90	Stress measurement under high pressure using Kawai-type multi-anvil apparatus combined with synchrotron radiation. Journal of Synchrotron Radiation, 2009, 16, 757-761.	2.4	7

#	Article	IF	CITATIONS
91	High pressure study of transition metal monoxides MnO and CoO: Structure and electrical resistance. Physics of the Earth and Planetary Interiors, 2014, 228, 170-175.	1.9	7
92	Formation of a metastable hollandite phase from amorphous plagioclase: A possible origin of lingunite in shocked chondritic meteorites. Physics of the Earth and Planetary Interiors, 2017, 272, 50-57.	1.9	7
93	Flow behavior and microstructures of hydrous olivine aggregates at upper mantle pressures and temperatures. Contributions To Mineralogy and Petrology, 2017, 172, 1.	3.1	7
94	Synchrotron X-ray diffraction observation of phase transformation during annealing of Si processed by high-pressure torsion. Philosophical Magazine Letters, 2021, 101, 223-231.	1.2	7
95	Direct Viscosity Measurement of Peridotite Melt to Lowerâ€Mantle Conditions: A Further Support for a Fractional Magmaâ€Ocean Solidification at the Top of the Lower Mantle. Geophysical Research Letters, 2021, 48, e2021GL094507.	4.0	7
96	Static compression of (Mg0.83,Fe0.17)O and (Mg0.75,Fe0.25)O ferropericlase up to 58 GPa at 300, 700, and 1100 K. American Mineralogist, 2012, 97, 176-183.	1.9	6
97	New phases of binary compounds: CsCl-type RuGe and RuSn. Europhysics Letters, 2014, 107, 56003.	2.0	6
98	Thermal expansion and P-V-T equation of state of cubic silicon nitride. Journal of the European Ceramic Society, 2019, 39, 3627-3633.	5.7	6
99	Hardness of polycrystalline SiO ₂ coesite. Journal of the American Ceramic Society, 2019, 102, 2251-2256.	3.8	6
100	Correlation Lengths of Linear and Branched Polymers in a Good Solvent. Polymer Journal, 1986, 18, 941-946.	2.7	5
101	Reaction boundary between akimotoite and ringwoodite + stishovite in MgSiO3. Physics and Chemistry of Minerals, 2017, 44, 425-430.	0.8	5
102	Nano-polycrystalline diamond synthesized from neutron-irradiated highly oriented pyrolytic graphite (HOPG). Diamond and Related Materials, 2018, 82, 132-136.	3.9	5
103	High-pressure and high-temperature synthesis of heavy lanthanide sesquisulfides Ln 2 S 3 (Ln =Yb and) Tj ETQq1	1 0,78431 5.5	.4 ₅ rgBT /Ow
104	Elastic wave velocities and Raman shift of MORB glass at high pressures. Journal of Mineralogical and Petrological Sciences, 2008, 103, 126-130.	0.9	5
105	Effects of Microwave Irradiation on Nonspecific Protein Binding in the Solid Phase Coated with Bovine Serum Albumin. Polymer Journal, 2005, 37, 109-117.	2.7	4
106	Development of an Anti-Analyte Ion Remover Used for Ion Chromatography: Part 1. Examination of a Device for Anion Analysis. Analytical Sciences, 2012, 28, 1071-1074.	1.6	4
107	Elastic wave velocity anomalies of anorthite in a subducting plate: In situ experiments. American Mineralogist, 2015, 100, 1856-1865.	1.9	4
108	Quenchable compressed graphite synthesized from neutron-irradiated highly oriented pyrolytic graphite in high pressure treatment at 1500 °C. Journal of Applied Physics, 2018, 123, 161577.	2.5	4

Үијі Нісо

#	Article	lF	CITATIONS
109	Sound Velocity of MgSiO 3 Majorite Garnet up to 18ÂGPa and 2000ÂK. Geophysical Research Letters, 2021, 48, e2021GL093499.	4.0	4
110	Low Velocity Zones in the Martian Upper Mantle Highlighted by Sound Velocity Measurements. Geophysical Research Letters, 2021, 48, e2021GL093977.	4.0	4
111	Selective removal of carbon dioxide contained in the effluent from ion chromatography suppressors using a new non-vacuum device. Journal of Chromatography A, 2015, 1392, 69-73.	3.7	3
112	Short-period cyclic loading system for <i>in situ</i> X-ray observation of anelastic properties at high pressure. Review of Scientific Instruments, 2016, 87, 105106.	1.3	3
113	Simultaneous generation of ultrahigh pressure and temperature to 50ÂGPa and 3300ÂK in multi-anvil apparatus. Review of Scientific Instruments, 2021, 92, 103902.	1.3	3
114	Sound velocity and density of liquid Ni68S32 under pressure using ultrasonic and X-ray absorption with tomography methods. Comptes Rendus - Geoscience, 2019, 351, 163-170.	1.2	2
115	Continuous measurement of ultrasonic elastic wave velocities, X-ray radiography and X-ray diffraction of Zr50Cu40Al10 metallic glass at high pressure and high temperature conditions. High Pressure Research, 2021, 41, 219-232.	1.2	2
116	Elastic wave velocities and Raman shift of MORB glass at high pressures — Reply. Journal of Mineralogical and Petrological Sciences, 2008, 103, 429-431.	0.9	2
117	Deformation of Postâ€Spinel Under the Lower Mantle Conditions. Journal of Geophysical Research: Solid Earth, 2022, 127, .	3.4	2
118	Equation of state of Ca2AlSiO5.5 oxygen defect perovskite. Physics and Chemistry of Minerals, 2015, 42, 327-336.	0.8	1
119	In-line System to Produce High-Purity Acid Solutions. Analytical Sciences, 2016, 32, 695-700.	1.6	1
120	Device to generate high purity hydroxide solution in-line for ion chromatography. Journal of Chromatography A, 2016, 1445, 105-111.	3.7	1
121	In-situ observation of the structural change in MgO-B2O3-SiO2 glass at high pressure and the permanent structural change. Journal of Non-Crystalline Solids, 2018, 499, 25-31.	3.1	1
122	Thermoelastic Properties of K0.7Na0.3AlSi3O8 Hollandite and NaAlSi2O6 Jadeite: Implication for the Fate of the Subducted Continental Crust in the Deep Mantle. Minerals (Basel, Switzerland), 2020, 10, 261.	2.0	1
123	Seismic Anisotropy in the Lower Mantle Transition Zone Induced by Lattice Preferred Orientation of Akimotoite. Geophysical Research Letters, 2022, 49, .	4.0	1
124	Phase boundary between cubic B1 and rhombohedral structures in (Mg,Fe)O magnesiowüstite determined by in situ X-ray diffraction measurements. Physics and Chemistry of Minerals, 2018, 45, 51-58.	0.8	0
125	Pressure effect on the electromotive force of the type R thermocouple. High Pressure Research, 2020, 40, 205-218.	1.2	0
126	In situ X-ray diffraction study on structural changes of neutron-irradiated highly oriented pyrolytic graphite under room- temperature compression and decompression. Diamond and Related Materials, 2022, 123, 108828.	3.9	0

#	Article	IF	CITATIONS
127	Overview of the High-Pressure Beamlines at SPring-8 and the Latest Research Results. Nihon Kessho Gakkaishi, 2022, 64, 33-40.	0.0	0
128	Exploration of the best reference material on anelastic measurement by cyclic loading under high pressure. High Pressure Research, 2022, 42, 14-28.	1.2	0